基于力觉遥示教曲线焊缝位置辨识方法

刘立君[1,2]， 高洪明[3]， 吴 林[3]

（1. 浙江大学 宁波理工学院，浙江 宁波 315100；2. 哈尔滨理工大学 材料科学与工程学院，哈尔滨 150080；
3. 哈尔滨工业大学 现代焊接生产技术国家重点实验室，哈尔滨 150001）

刘立君

摘 要：在遥控焊接环境中，时常碰到具有一定曲率的曲线焊缝，曲线焊缝精确辨识是保证遥示教精度前提条件之一。针对曲线焊缝的特点，提出了焊缝拐点和方向系数概念，并建立了曲线焊缝辨识方向系数智能控制模型，结合焊缝拐点识别算法，进行曲线焊缝辨识试验。结果表明，实现了曲线焊缝拐点自动识别，为遥示教曲线焊缝拐点识别提供了一种新方法。将力觉曲线焊缝辨识试验曲线上传给离线编程系统，由离线编程系统对焊缝拐点进行优化处理后，非常接近实际焊缝曲线，最大误差不超过 ±0.5 mm，能够满足遥控焊接遥示教要求。

关键词：遥控焊接；遥示教；力觉；曲线焊缝

中图分类号：TP242 文献标识码：A 文章编号：0253－360X(2008)08－0093－04

0 序 言

在核设施修复、空间站装配和海洋工程建设等需要有人参与进行遥控焊接，遥控示教是遥控焊接的关键技术之一[1]。传统的焊接机器人示教无法满足遥控焊接工艺要求[2－4]，希望研发出新的遥控焊接遥示教方法，其中激光视觉传感辅助示教是新提出的遥示教方法，但也无法适应所有遥控焊接环境，如工件表面状态对激光辅助示教有一定影响，不规则焊缝特征点提取困难[5]。所以希望开发新的遥示教方法，以便解决不同遥控焊接条件下遥示教问题。将力觉引入遥控焊接遥示教中，与立体视觉配合，能够完成遥控焊接遥示教任务，且信息处理不复杂，不受环境光、烟、气雾、色彩等的干扰，在激光视觉遥示教看不清场合仍能“摸”得出[6－8]。曲线焊缝辨识在遥控焊接遥示教具有一定普遍意义，文中提出利用力觉辨识曲线焊缝，特别是焊缝拐点辨识方法，在实际遥示教中取得较好应用效果。

1 力觉曲线焊缝点间变迁算法

假设焊缝为 xSy 平面曲线焊缝，在 xSy 平面内由示教点 P_i 向下一个示教点 P_{i+1} 变迁方向为当前示教点 P_i 切线方向，该切线段与实际焊缝轨迹的偏差最小。切线方向由探针与焊缝坡口接触时的受力情况确定，如图 1 所示，F_{ix} 为第 i 个示教点在六维力坐标系 x 轴方向所受的力，F_{iy} 为第 i 个示教点在六维力坐标系 y 轴方向所受的力，F_{ixy} 为第 i 个示教点的 F_{ix} 和 F_{iy} 在六维力坐标系中 xSy 平面内所产生的合力。在 y 向作试探性进给，产生 F_{ix} 和 F_{iy} 力信号，合力为 F_{ixy}，与切线方向垂直，通过 F_{ixy} 确定切线在 xSy 平面内方向。在搜索过程中，如果连续两次合力 F_{xy} 反向，则要减小进给量大小，避免超调，破坏力传感器。搜索进给量可用下式估算

$$\left.\begin{aligned}\Delta Y_i &= L \cdot |F_{ix}| / |F_{ixy}| \\ \Delta X_i &= L \cdot (-F_{iy}) / |F_{ixy}|\end{aligned}\right\} \tag{1}$$

式中：L 为搜索进给的步长，可取 0.4 ~ 0.8 mm。如果 F_{ixy} 近似等于 0，则试探方向及位焊缝轨迹切向，取 $\Delta X_i = 0$，$\Delta Y_i = L$。ΔY_i 的正负决定了搜索的方向，当示教点轨迹切线矢量与力传感器 y 轴夹角在 $[0,\pi]$，取正号，在 $[\pi, 2\pi]$ 内，取负号。ΔX_i 式中 F_{iy} 表示在力传感器坐标系中 y 轴方向力，大小等于 $|F_{iy}|$，正负取决于所受力是否与 y 轴同向，方向相同为正，相反为负，可从力传感器中直接读出。试探性进给仅用于示教起始点进给量计算，其余示教点变迁搜索进给量 ΔY_{i+1}，ΔX_{i+1}（示教点 $i = 2, 3, 4\cdots\cdots$）由上一个示教点搜索进给量 ΔY_{i-1}，ΔX_{i-1}，当前示教点切向进给计算量 ΔY_i，ΔX_i 和 F_{ixy} 力向调整量 ΔY_{ixy}，ΔX_{ixy} 加权组成。

收稿日期：2007－10－22

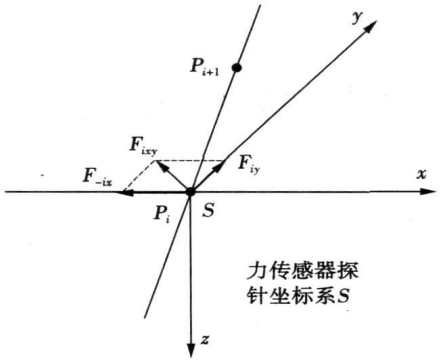

图 1 曲线焊缝任意点受力示意图

Fig. 1 Sketch of forced point on curve welding seam

$$\left.\begin{aligned}\Delta Y_{i+1} &= m \cdot \Delta Y_i + n \cdot \Delta Y_{i-1} + k \cdot \Delta Y_{ixy}\\ \Delta X_{i+1} &= m \cdot \Delta X_i + n \cdot \Delta X_{i-1} + k \cdot \Delta X_{ixy}\end{aligned}\right\} \quad (2)$$

式中：权数 m, n, k 的和为1。切向进给计算量 ΔY_i 的正负号取与上一个示教点搜索进给量 ΔY_{i-1} 的符号相同，n 取0.3 ~ 0.5。F_{xy} 力向调整量 ΔY_{xy} 旨在使力传感器探针保持趋于焊缝轨迹中心线的倾向，方向与 F_{xy} 相同，k 取 0.1 ~ 0.2。

为了有效识别曲线焊缝不同曲率，首先定义遥示教点方向系数

$$\left.\begin{aligned}R_{ix} &= |F_{ix}| / |F_{ixy}|\\ R_{iy} &= |F_{iy}| / |F_{ixy}| \text{（示教点 } i = 1, 2, 3 \cdots n)\end{aligned}\right\} \quad (3)$$

当前方向系数 R_{ix}, R_{iy} 与上次方向系数 $R_{(i-1)x}$, $R_{(i-1)y}$ 差值的绝对值 ΔR_{ix} 和 ΔR_{iy} 超过规定值，则断定曲线焊缝轨迹出现拐点。

$$\left.\begin{aligned}\Delta R_{ix} &= |R_{ix} - R_{(i-1)x}| \geqslant \arccos x_i\\ \Delta R_{iy} &= |R_{iy} - R_{(i-1)y}| \geqslant \arccos y_i\end{aligned}\right\} \quad (4)$$

取切向进给计算量 ΔX_i, ΔY_i 作为拐点处示教点搜索进给量，若实施驱动后到 $i+1$ 点，此时如果

$$\left.\begin{aligned}\Delta R_{(i+1)x} &= |R_{(i+1)x} - R_{(i)x}| \geqslant \arccos x_i\\ \Delta R_{(i+1)y} &= |R_{(i+1)y} - R_{(i)y}| \geqslant \arccos y_i\end{aligned}\right\} \quad (5)$$

说明没有进入拐点后新焊缝轨迹，取此时切向进给计算量 $\Delta X_{i+1} = -\Delta X_i$, $\Delta Y_{i+1} = -\Delta Y_i$ 控制机器人带动探针进入拐点后的新焊缝轨迹，在拐点处应该调整探针姿态，以便进入一个新的焊缝轨迹。

2 力觉曲线焊缝位置辨识试验

试验装置见图 2，轨迹曲率半径225 mm，机器人运动精度 ±0.1 mm，搜索进给步长0.3 ~ 0.9 mm，根据方向系数偏差 R_{ix}, R_{iy} 和偏差变化率 ΔR_{ix}, ΔR_{iy}，推测下一个示教点所在焊缝轨迹曲率大小，曲率小，选择搜索步长取对应大值，曲率大，选择搜索步长取对应小值。

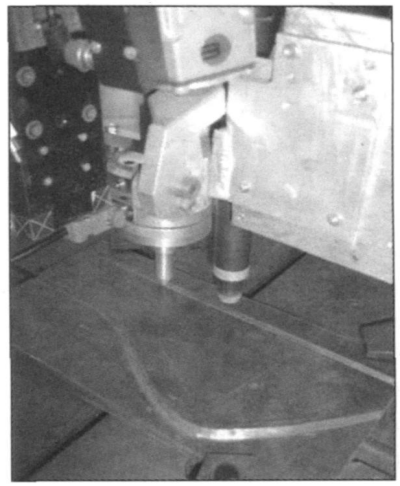

图 2 曲线焊缝位置辨识试验装置

Fig. 2 Position identifying experiment set of curve welding seam

曲线焊缝起始点确定是在视觉引导下，找到起始示教点 P_1 位置后，如图3 所示，在视觉引导下，通过操作者人工操作，初步确定起始示教点姿态，然后根据力觉曲线焊缝点间变迁控制方法，搜索焊缝轨迹下一点 P_2，找到 P_2 的判断原则是根据方向系数（根据不同曲率设定，包括拐点值设定），如果无变化或在一定阈值范围内，则认为是直焊缝，不调整姿态，如果变化超过一定曲度对应规定值，则认为到达 P_2 点，在 P_1 ~ P_2 段内认为是直坡口，姿态相同。由示教点 P_1 到示教点 P_2 搜索具体步骤：首先根据 z 向的 F_z 大小和变化值控制探针沿力传感器探针坐标系 S 的 z 正向进给或负向进给，始终保持一定范围的接触力 F_z，如果 z 进给变化值达到需要姿态调整规定值，则进入姿态调整子程序。如果 z 进给变化值在准许范围内，则在 y 向作试探性进给，根据 F_{ix} 和 F_{iy} 力信号合力 F_{ixy} 确定切线在 xSy 平面内方向，根据搜索进给量估算式(1)，计算 ΔX_1 和 ΔY_1，输出驱动遥控焊接从机器人搜索进给运动，再根据对进给方向系数的动态过程变化趋势监测，采取不同控制步长，提高了方向辨识精度和效率。

因机器人每次都是在 y 方向作试探性进给，再根据当前遥示教点方向系数确定下一步进给方向和进给步长，由式(3) 方向系数定义可知，只要计算出 y 方向遥示教点方向系数即可知道 x 方向系数，即

$$R_{ix} = 100\% - R_{iy} \quad (6)$$

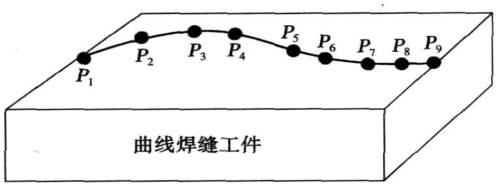

图 3　曲线焊缝示教点位置模型

Fig. 3　Teaching model of curve welding seam

因此只要通过 y 方向遥示教点方向系数偏差和偏差变化率判断机器人搜索步长大小即可，当然也可以用 x 方向遥示教点方向系数偏差和偏差变化率判断机器人搜索步长大小。图 4 为基于方向系数变化机器人搜索步长推理控制模型，横坐标代表 y 方向进给方向系数偏差 ΔR_{iy}，纵坐标代表 y 方向进给方向系数偏差变化率 $\Delta(\Delta R_{iy})$，$f(\Delta R, \Delta(\Delta R))$ 代表进给方向系数变换轨迹。

$$\Delta R_{iy} = R_{iy} - R_{(i-1)y} \tag{7}$$

$$\Delta(\Delta R_{iy}) = \Delta R_{iy} - \Delta R_{(i-1)y} \tag{8}$$

根据当前示教点在 y 方向进给方向系数偏差和偏差变化率在图 4 中的位置，推测下一个示教点所在焊缝轨迹曲率大小，曲率小，选择搜索步长取对应大值；曲率大，选择搜索步长取对应小值。

如图 4 所示，在方向系数偏差较大和偏差变化率大于零时，对应图 4 区域①和⑦，说明焊缝曲率变化较大，步长取小值0.3 mm。在方向系数偏差和方向系数偏差变化率均很小，说明焊缝曲率变化较小，这段焊缝近似直焊缝，对应区域⑥，可采取大的步长

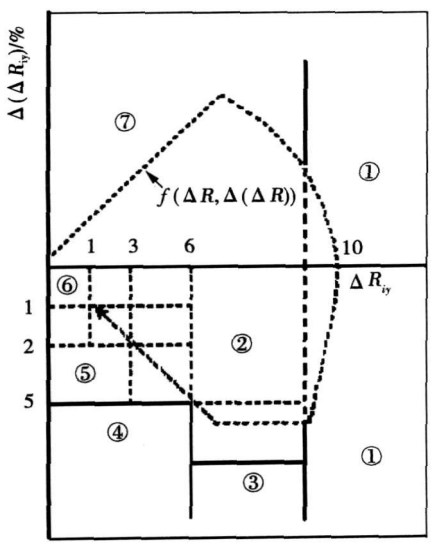

图 4　基于方向系数变化机器人搜索步长推理控制模型

Fig. 4　Control model of robot searching step length based on the direction coefficient

0.7～0.9 mm，以便提高效率。在方向系数偏差减小过程中，若方向系数偏差变化速度低于或等于预定速度时，对应区域②，可采取步长0.4 mm。若方向系数偏差变化速度大于预定速度时，对应区域③和⑤，可采取步长0.5 mm。若方向系数偏差变化速度还没有减小到预定速度范围，对应区域④，可采取大的步长0.6 mm。上述调整是在假设前后两点不超过 8°变化情况下进行的，即方向系数为 0.1。如果超过 8°，则断定到达焊缝轨迹示教点 P_2。利用式(2)计算 $P_2 \sim P_3$ 搜索进给量，重复上述步骤，直到辨识结束。

为与焊缝受力信号坐标定义一致，定义图 5 横坐标代表焊缝长度，与 F_{ix} 空间笛卡尔坐标系 x 方向相同。纵坐标代表焊缝宽度，与 F_{iy} 空间笛卡尔坐标系 y 方向相同。由图可以看出，将力觉曲线焊缝辨识试验曲线上传给离线编程系统，由离线编程系统对焊缝拐点进行优化处理后，非常接近实际焊缝曲线，最大误差不超过 ±0.5 mm，满足遥控焊接遥示教曲线焊缝辨识精度要求。

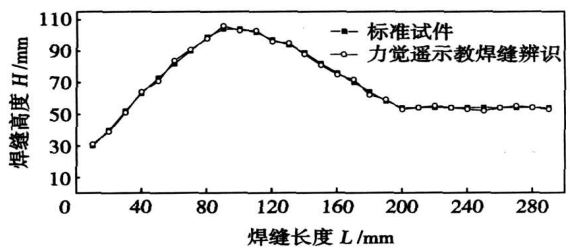

图 5　曲线焊缝位置辨识试验

Fig. 5　Identifying experiment of the position of curve welding seam

3　结　　论

(1) 针对具有拐点曲线焊缝辨识，提出了遥示教点方向系数概念和焊缝拐点识别算法，并建立了曲线焊缝辨识方向系数仿人智能控制模型，为曲线焊缝快速识别奠定基础。

(2) 根据曲线焊缝拐点识别算法和方向系数仿人智能控制模型，进行曲线焊缝辨识试验，试验结果表明，经过将力觉曲线焊缝辨识试验曲线上传给离线编程系统，由离线编程系统对焊缝拐点进行优化处理后，非常接近实际焊缝曲线，拐点处最大误差不超过±0.5 mm，满足遥控焊接遥示教曲线焊缝辨识精度要求。

参考文献：

[1] 张惠斌，周振丰，吴 林，等. 遥控弧焊机器人系统[J]. 焊接学报，1995，16(3)：153－157.

[2] 周 鲲，邵 华. 焊接机器人的示教轨迹优化[J]. 机械设计与制造，2003(4)：46－47.

[3] 吴 威，赵 杰，王晓东，等. 焊接机器人在线示教[J]. 焊接学报，1995，16(1)：16－19.

[4] 张爱红，张秋菊. 基于虚拟现实技术的机器人示教方法[J]. 江南大学学报，2003，2(3)：258－261.

[5] 李海超，吴 林，高洪明，等. 应用于遥控焊接的激光视觉传感辅助遥控示教[J]. 焊接学报，2006，27(5)：39－42.

[6] Chul H I, Chul H M. Robust hybrid position/force control with adaptive scheme[J]. JSME International Journal, Series C: Mechanical Systems, Machine Elements and Manufacturing, 2004, 47(4): 1161－1165.

[7] Renzo D, Alberto D M. Comparison of contact-force models for the simulation of collisions in DEM-based granular flow codes[J]. Chemical Engineering Science, 2004, 59(3): 525－541.

[8] 吴 林，孔 宇. 焊接位置与焊丝方位定义的讨论及几何建模研究[J]. 机械工程学报，1997，33(5)：49－53.

作者简介：刘立君，男，1968 年出生，博士，教授，硕士生导师，黑龙江省中小企业咨询专家委员会委员。主要从事焊接自动控制方面的科研和教学工作。发表论文 60 余篇。

Email：888liulijun@163.com

[上接第 92 页]

有明显的改善作用。由于磷替代了锌被氧化，而形成的 P_4O_6 易于挥发，因此焊料表面形成的氧化层厚度更小，更有利于焊料的润湿。

(2) 经过氧化后，由于合金中磷含量减少，组织中粗大的富锌相减少，因此合金的断后伸长率提高。

(3) 当合金中 P 元素含量为 0.2%时，焊料的综合性能最好。经长时间氧化后，焊料的润湿性仍然优于 Sn-8Zn-3Bi 焊料。这对于该焊料应用于波峰焊是十分有益的。

参考文献：

[1] 史益平，薛松柏，王俭辛，等. 稀土元素 Ce 对 Sn-Cu-Ni 无铅钎料铺展性能及焊点力学性能的影响[J]. 焊接学报，2007，28(11)：73－78.

[2] Suganuma K, Kim K S. Sn-Zn low temperature solder[J]. Journal of Materials Science, 2007, 18(1－3): 121－127.

[3] Suganuma K. Current technology of low temperature lead-free soldering and JIEP project[C] // International Canference on Lead Free Electronics "Iowant Impermentation of the RHS Directive", IPC/Solder tech, Brussels, 2003: 97－104.

[4] Huang Chiawei, Lin Kwanglung. Morphology of intermetallic compounds formed between lead-free Sn-Zn based solders and Cu substrates[J]. Journal of Electronic Materials, 2006, 35(12): 2135－2141.

[5] Sungil Cho, Jin Yu, Sung K. *et al*. The oxidation of lead-free Sn alloys by electrochemical reduction analysis[J]. Journal of the Minerals Metals &Materials Society, 2005(6): 50－52.

[6] Xian Aiping, Gong Guoliang. Oxidation behavior of molten tin doped with phosphorus[J]. Journal of Electronic Materials, 2007, 36(12): 1669－1678.

[7] 李铁藩. 金属高温氧化和热腐蚀[M]. 北京：化学工业出版社，2003.

作者简介：方伊莉，女，1985 年出生，硕士研究生。主要从事无铅焊料的研究。

Email：Jethro@seu.edu.cn

p73—76

Abstract: Finite element method is used to analysis the soldered joint reliability of FCBGA, the unified viscoplastic Anand constitutive equation is employed to represent the viscoplastic deformation behavior of Sn63Pb37 alloy. The results shows that the stress concentrated on the top surface of the chip-edge FCBGA corner soldered joint and present cyclical changes with time, stress relaxation and accumulated enhancement trend of stress can be obvious acquired from the curve. Select three different ball size device for the study, it indicates that the ball size of 0.4 mm × 0.28mm has the maximal soldered joint stress, 0.46 mm × 0.34mm ball second, and 0.52 mm × 0.4mm ball minimum. Based on the analysis of plastic work accumulation can acquire the same trend. The trends is obtained by the consistent results with practical application of the device. At the same time provide a basis for the theoretical research of flip-chip devices.

Key words: FCBGA; finite element method; viscoplastic; stress concentration

Verification of ultrasonic residual stress evaluation method by laser hologram method LU Hao, LIU Xuesong, YANG Jianguo, FANG Hongyuan, ZHOU Guangtao, YAN Dejun (State Key Laboratory of Advanced Welding Production Technology, Harbin Institute of Technology, Harbin 150001). p77—79

Abstract: Based on the acoustoelasticity, the residual stress can be measured by ultrasonic method. Experimental system to measure the residual stress by ultrasonic is established with Lcr waves. The longitudinal stress of twin wire welded plate is measured by the system. The result of the ultrasonic method is verified by laser hologram interference hole-drilling method. The measurement processes of two methods are compared. The measurement process is not only nondestructive, but also real-time and quick. The system is portable and overcomes the shortcomings of the tradition methods.

Key words: ultrasonic; laser hologram; welding residual stress

Microstructures and mechanical properties of CGHAZ in 440 MPa ship hull steel YANG Yinhui[1,2], YANG Caifu[2], SU Hang[2], ZHANG Yongquan[2], CHAI Feng[2], DAI Jianqing[1] (1. Kunming University of Science and Technology, Kunming 650093, China; 2. Central Iron and Steel Research Institute, Beijing 100081, China). p80—84

Abstract: The results showed that the austenite grain size in low carbon high niobium (LCHN) alloy steel was smaller than that in high carbon low niobium steel (HCLN) by adopting welding heat physical simulation, and the low temperature impact toughness of LCHN steel was higher than that in the HCLN steel when $t_{8/5} \leqslant 40$ s. The microstructure of coarse grain heat affected zone (CGHAZ) in experimental steels were predominantly granular bainite, the shape of M-A island exhibited long lath morphology when $t_{8/5} \leqslant 40$ s and it shows massive morphology when $t_{8/5} > 40$ s. The size and the amount of granular bainite in LCHN steel were much lower than that in HCLN steel. The precipitation equilibrium diagrams of two experimental steels were calculated by using Thermo-Calc software. The second phase particles mainly precipitated in the temperature higher than 1 200 ℃ and the mean size of particles larger than 120 nm in HCLN steel, but the second phase particles only precipitated in the temperature lower than 1 200 ℃ and the mean size of particles lower than 50 nm in LCHN. The fine second phase precipitation dispersed in LCHN steel inhibited the growth of prior austenite grain boundary and improved the low temperature impact toughness significantly.

Key words: coarse grain heat affected zone; grain size; granular bainite; the second phase particles

Content of Fe in TIG cladding copper alloy layer on surface of steel LÜ Shixiong, SONG Jianling, YANG Shiqin (State Key Laboratory of Advanced Welding Production Technology, Harbin Institute of Technology, Harbin 150001, China). p85—88

Abstract: TIG cladding was carried out on the surface of 35CrMnSiA steel using HS201 welding wire. The content of Fe in the cladding layer and the microstructure of the interface between copper layer and base metal were analyzed. The evolvement and development of the distribution and the shape of the Fe in the cladding layer was investigated systemically. The results show that with the increased welding current, the content of Fe is increased and the shape is transformed greatly. The shape of Fe is granular and treeing-like in the cladding layer with the welding current below 270A; the shape of Fe is changed strongly and the large spherical Fe particle appears in the cladding layer with the welding current surpassing 300 A. Under the effect of the arc force, the liquid Cu and Fe is mechanically mixed and the configuration of the solidified microstructure is the inclusion of Cu and Fe.

Key words: TIG cladding; 35CrMnSiA steel; copper welding wire; content of Fe

High-temperature oxidation behavior of Sn-8Zn-3Bi-P and its effect on properties FANG Yili, ZHOU Jian, XUE Feng, SUN Yangshan (Jiangsu Key Laboratory for Advanced Metallic Materials, Southeast University, Nanjing 211189, China). p89—92, 96

Abstract: The effect of alloying P on oxidation behavior of the liquid Sn-8Zn-3Bi lead-free solder at 250 ℃ was investigated by thermogravimetry experiment. The effect mechanism of P on the oxidation was discussed by scanning electronic microscopy (SEM) and auger electronic spectroscopy (AES) in experiments. Properties were compared between before after oxidation to explore the effect on solders' other properties. The results indicate that P can improve the oxidation resistance of Sn-8Zn-3Bi obviously. P was oxidized which is prior to Zn. A oxide film consisting of P_4O_6 which was tend to volatilize formed on the surface of the solder. The over-all properties of the solder is best with the addition of 0.2wt. %P.

Key words: Sn-8Zn-3Bi; lead-free solder; P; oxidation resistance; mechanism

Position identifying of curve welding seam in tele-teaching based on force sensing LIU Lijun[1,2], GAO Hongming[3], WU Lin[3] (1.

Ningbo Institute of Technology, Zhejiang University, Ningbo, Zhejiang 315100, China; 2. School of Material Science & Engineering, Harbin University of Science and Technology, Harbin 150080, China; 3. State Key Laboratory of Advanced Welding Production Technology, Harbin Institute of Technology, Harbin 150001, China). p93—96

Abstract: There often be the curve welding seam (CWS) in remote welding. The accurately identified CWS is one of the prerequisites to ensure tele-teaching precision. Aiming at the characters of CWS, the concept of inflection point and direction coefficient of welding seam are put forward. The intelligent model of direction coefficient of welding seam is established. Combining with the identifying algorithm of inflection point in welding seam, identifying experiment of CWS is done. The experiment results show that inflection point of welding seam can be automatically identified, that the average error of CWS is less than ±0.5 mm by optimal treatment of offline programming system, and meets the requirements of tele-teaching.

Key words: remote welding; tele-teaching; force sensing; curve welding seam (CWS)

Identification of multiclass defects in aluminum alloy resistance spot welding based on support vector machine XUE Haitao[1], LI Yongyan[1], CUI Chunxiang[1], AN Jinlong[2] (1. School of Materials Science and Engineering, Hebei University of Technology, Tianjin 300132, China; 2. School of Electrical Engineering and Automation, Hebei University of Technology, Tianjin 300132, China). p97—100

Abstract: A model is built to identify splash defect and incomplete fusion defect of aluminum alloy resistance spot welding based on Support Vector Machine method. The characteristic vector used in the model is extracted from process curves of aluminum alloy resistance spot welding. This model is trained and tested with different sample data. The test result shows that the accuracy rate of identifying splash defect is 96.7% and the accuracy rate of identifying incomplete fusion defect is 100% under given sample data. Therefore, it is reliable to identify multiclass defects of aluminum alloy resistance spot welding with Support Vector Machine method.

Key words: aluminum alloy resistance spot welding; support vector machine; defect identification

Influence of loading of tensile stress on welding residual stress field in plate structure PAN Hua[1], FANG Hongyuan[2] (1. Automobile Steel Department, Research Institute, Baoshan Iron & Steel Corporation Limitid Shanghai 201900, China; 2. State Key Laboratory of Advanced Welding Production Technology, Harbin Institute of Technology, Harbin 150001, China). p101—104

Abstract: By finite element method (FEM), the distribution of welding residual stress field in the plate structure was investigated under the condition of local loading, and compared the results of reducing stress between tension in process of welding and after welding. It is found that under the condition of local loading, tension in welding process can decrease the residual stress more significantly than that after welding. When the local loading was lower than the yield strength of the material, the decrease of residual stress become more prominence as the local loading increasing. When 200 MPa loading was applied, the maximum tension residual stresses decreases to 130 MPa after welding and to 50 MPa during welding. These results indicate that the decrease of welding residual stress by local loading is feasible.

Key words: welding; residual stress; finte element method; mechanical tension

Microstructure and properties of E911 steel welded joint aged at 650 ℃ for long-time REN Wenchao[1], GONG Zhengchun[2], CHANG Tiejun[3], WANG Chunbin[3] (1. School of Mechanical and Electrical Engineering, Harbin Engineering University, Harbin 150001, China; 2. Harbin Boiler Company Ltd, Qinhuangdao Hebei 066206, China; 3. College of Materials Science and Chemical Engineering, Harbin Engineering University, Harbin 150001, China). p105—108

Abstract: The mechanical properties, serial impact and sustained strength of the welded joint aged at 650 ℃ for long-time of E911 steel produced by German Vallourec & Mannesmann were tested, optical microscope, transmission electron microscope (TEM) and scanning electron microscope (SEM) were used to observe and analyze the microstructures and the fracture apptarance. The tests show that the welded joint aged at 650 ℃ for long time of E911 steel has good mechanical properties and sustained strength, the rupture strength of E911 steel is 72.52 MPa when the aging time is extended to 100,000 hours at 650 ℃, and the rupture strength of welded joint is 60.88 MPa.

Key words: E911 steel; long-time aging; sustained strength; microstructure; mechanical properties

3D finite element simulation on distortion distribution in multi layers welding of EH36 CHEN Zhanglan, XIONG Yunfeng, LI Zongmin (Marine Engineering School Jimei University, Xiamen, Fujian 361021, China). p109—112

Abstract: As one of low temperature high strength steel, EH36 is widely used in key construction of ship. Based on the thermal-physical properties of EH36, 3D finite element simulation is carried out to analyse the temperature field and distortion distribution. To simulate the actual welding process, some technologies, such as APDL program used for development and birth & death skill, are applied in 3D multi passes welding. Thus the temperature field and weld distortion distribution in 3-directions are obtained. The result of simulation shows that there are many different distortions between the first pass and the second one, and that difference lies between the firstly welded part first and the later welded part. Further, the distortions of U-shape groove and V-shape groove were compared, the angle deformation of workpieces with V-shape groove is obviously greater than that of the U-shape groove at the same area of weld crass-section, both of them share with the same areas, same welding process and simulation process.

Key words: EH36 steel; multi-layers; distortion; simulation